MOX-Report No. 93/2023

Optimal surface clothing with elastic nets

Andrini, D.; Magri, M.; Ciarletta, P.

MOX, Dipartimento di Matematica
Politecnico di Milano, Via Bonardi 9 - 20133 Milano (Italy)

mox-dmat@polimi.it https://mox.polimi.it

Optimal surface clothing with elastic nets

D. Andrini, M. Magri and P. Ciarletta

[1] MOX, Department of Mathematics, Politecnico di Milano, Piazza Leonardo da Vinci 32, 20133 Milano, Italy

Abstract

The clothing problem aims at identifying the shape of a planar fabric for covering a target surface in the three-dimensional space. It poses significant challenges in various applications, ranging from fashion industry to digital manufacturing. Here, we propose a novel inverse design approach to the elastic clothing problem that is formulated as a constrained optimization problem. We assume that the textile behaves as an orthotropic, nonlinear elastic surface with fibers distributed along its warp and weft threads, and we enforce mechanical equilibrium as a variational problem. The target surface is frictionless, except at its boundary where the textile is pinned, imposing a unilateral obstacle condition for the reactive forces at the target surface. The constrained optimization problem also accounts for an elongation condition of the warp and weft fibers, possibly with bounded shearing angle. We numerically solve the resulting constrained optimization problem by means of a gradient descent algorithm. The numerical results are first validated against known clothing solutions for Chebyshev nets, taking the limit of inextensible fibers. We later unravel the interplay between thread and shear stiffness for driving the optimal cloth shape covering the hemisphere and the hemicatenoid. We show how the metric of these target surfaces strongly affects the resulting distribution of the reaction forces. When considering the limit of covering the full sphere, we show how clothing with elastic nets allows to avoid the onset of singularities in the corresponding Chebyshev net, by developing corners at the cloth boundary.

1 Introduction

The use of elastic nets for clothing a given surface is widespread in several application encountered in everyday life, as illustrated in Fig. 1. However, covering arbitrary surfaces in a three-dimensional (3D) space with planar fabrics and textures poses a significant challenge in various industrial and scientific domains, including the composite [1] and the fashion [2] industries, as well as in the emerging field of 4D printing [3]. The manufacturing process leading to the final 3D surface may be executed through manual assembly,

Figure 1: Examples of deforming planar elastic nets into three-dimensional surfaces: (a) preform of a textile reinforcement for composite materials (adapted from [4]); (b) elastic fishnet socks; (c) foam mesh nets for fruit shock protection.

with or without guide surfaces, or by harnessing diverse actuating systems. Manual assembly methods are

involved in processes like creating preforms for textile-reinforced composites and crafting garments from two-dimensional (2D) patterns. Alternatively, automated shape transformation and assembly techniques can be employed, such as thermal-responsive origami structures [5] and shape-morphing inflatables [6]. The initially 2D planar material can be manufactured by conventional means like weaving and knitting, or via 3D printing [7]. Whenever the target surface is non-developable, mechanical stresses occur due to elastic distortions arising in the forming stage.

Designing the shape transformation is often a backward approach from the manufacturing process, where the shape of the initial planar material is determined starting from the 3D target surface, taking into account given physical constraints. Hence, the problem is often conceptualized as an *inverse design process* [8]. Several theoretical studies has been done on the subject [9, 10] with applications to the design of tires [11], turbine-blades [12], and bio-mechanical devices [13].

From a continuum mechanics perspective, the inverse design method is grounded on the so-called *inverse deformation problem* [14], with the aim to determine the undeformed, stress-free, configuration of a body, given its deformed state and applied traction and body forces. Over the past decades, numerous theoretical and computational techniques have been proposed for solving inverse elasto-static problems (e.g. [15, 16, 17, 18]). Among them, Lagrangian approaches impose equilibrium in the deformed configuration [15], while Lagrangian-Eulerian formulations are able to account for an arbitrary reference configuration [17]. For both approaches, the resulting non-linear equations can be solved either directly, for example, through the Finite Element method, or iteratively, by means of optimization algorithms as in [19, 20].

One of the first attempts to solve the inverse design problem of surface clothing by means of textiles dates back to Chebyshev [21], who developed a purely geometrical model. In Chebyshev nets, the interwoven fabric is idealized as a network of inextensible threads. Using this simple idea, Chebyshev was able to derive analytically the shape of a cloth patch covering a hemisphere. Later, Servant [22, 23] showed that clothing a generic surface with a Chebyshev net involves a system of two hyperbolic partial differential equations that are difficult to solve analytically, unless for specific shapes such as the surfaces of revolution [24, 25]. Additional challenges involve the appearance of geometric singularities, particularly those arising from local fiber collapse, e.g. those inevitably occurring while covering the sphere [26]. Such singularities can be typically circumvented by assembling the fabrics using multiple patches sewn together. Later, the Chebyshev net model was enhanced to incorporate the elastic behavior of the fabric [27, 28], accounting for threads extension [29], shear rigidity [30], bending stiffness [31] and twisting [32]. In addition to the aforementioned works, significant progress in the mechanical modelling of textiles has been driven by the composite industry [1] leading to the development of new accurate constitutive laws [33, 34, 35, 36].

Computational modeling of inverse design of textile materials has also received significant attention from the computer graphics community. A number of studies focused on automatically generating 2D sewing patterns from a given 3D model of a garment, as in [37, 38, 39, 40]. Most of these studies propose purely geometrical approaches. A few assume that the cloth is only capable of sustaining "quasi-isometric" transformations [41, 42]. Hence, the target 3D surface is divided into patches, designed to minimize a target measure of their distortion once flattened onto a plane, in order to generate 2D sewing patterns. Geometric approaches to cloth patch design have also been extended so as to allow for changes in the shear angles between the threads, by means of Chebyshev nets [43, 44]. In doing so, the authors were able to better emulate the anisotropic response typical of woven fabrics. Finally, further models considered physically-based approaches to get a more realistic description of cloth mechanics and cloth-body interactions (e.g. [45, 46, 47, 48]). Notable contributions considered a strain energy decomposition into in-plane stretch, along the warp and weft directions, and shear effects to model the mechanics of woven fabrics [45, 47]. On the contrary, an isotropic hyperelastic membrane model has been proposed for modeling the optimal design of skintight clothes [48] .

Despite these noticeable results in the state-of-the-art, most existing works rely on multiple approximations on the mechanical response in order to reduce the computational effort of simulating the fabric response efficiently. Here, we propose a mechanically rigorous approach to the clothing problem, developing a robust computational framework to derive an optimal shape of elastic textiles for covering a given surface, for applications to additive manufacturing and optimal design of conventional textiles.

The remainder of the paper is organized as follows. In Section 2, we set the notation and the functional setting of our optimal clothing problem. In Section 3, we define the main geometric and mechanical assumptions for deriving the corresponding mathematical model as a constrained optimization problem. In Section 4, we describe the numerical implementation of the model. The numerical results are presented in Section 5

for several test cases. In Section 6, we finally resume some critical discussion and concluding remarks.

2 Optimal clothing problem

2.1 Notation and problem setting

Let us consider an infinitely extended textile $\mathscr{T}$, $\mathcal{M}$ being a bounded region of it by which we aim at covering a given target surface $\mathcal{N}$.

We model the textile as a two-dimensional continuous body, described by a surface immersed in the three dimensional Euclidean space $\mathbb{E}^3$. We assume its reference relaxed configuration $\mathscr{T} \subset \mathbb{E}^3$ to be planar. Hence, upon fixing a *reference* orthonormal basis $\mathbf{E}_i$, i=(1,2,3), for $\mathbb{E}^3$, for the ease of notation we identify $\mathscr{T}$ with the subspace of $\mathbb{E}^3$ spanned by the basis $\mathbf{E}_1$ and $\mathbf{E}_2$. In addition, the set $\mathscr{T}$ is equipped with two tangent vector fields $\mathbf{v}$ and $\mathbf{w}$ whose integral lines represent warp and weft threads of the textile. In particular, we assume that the warp and weft lines are straight and mutually orthogonal in the reference configuration. Hence, it is convenient to set $\mathbf{v} = \mathbf{E}_1$ and $\mathbf{w} = \mathbf{E}_2$ to fix the spatial orientation of the patch, introducing the corresponding structural tensors $\mathsf{V} = \mathbf{E}_1 \otimes \mathbf{E}_1$ and $\mathsf{W} = \mathbf{E}_2 \otimes \mathbf{E}_2$.

The flat patch $\mathcal{M}$ undergoes an elastic deformation $\mathbf{f} : \mathcal{M} \to \mathbb{E}^3$ in order to cover the target surface $\mathcal{N}$, namely

$$\mathbf{f}(\mathcal{M}) = \mathcal{N} \qquad (\textit{target shape condition}).$$

To ensure coverability, the target surface $\mathcal{N}$ is assumed to be orientable with unit normal vector denoted by $\mathbf{n}$. Moreover, we assume that the orientation of $\mathbf{n}$ indicates the side of the target surface that can be covered. Specifically, $\mathbf{n}$ is chosen to point towards the region of space through which the textile can approach $\mathcal{N}$. We denote with $\mathbf{X} = (X_1, X_2)$ the coordinates of the material position in the reference fabric $\mathscr{T}$ written with respect to $\mathbf{E}_\alpha$, $\alpha = (1, 2)$. Moreover, upon introducing the *current* orthonormal reference frame $\mathbf{e}_i$, $i = (1, 2, 3)$, we indicate with $\mathbf{x} = (x_1, x_2, x_3)$ the coordinates for the spatial counterpart of $\mathbf{X}$, i.e. $\mathbf{x} = \mathbf{f}(\mathbf{X})$.

We then introduce the differential of the map $\mathbf{f}$ as $\mathsf{F} = (\partial_{X_\alpha} f_i)\mathbf{e}_i \otimes \mathbf{E}_\alpha$ where f_i denotes the i-th component of the map $\mathbf{f}$ [49]. There, we embrace the Einstein convention of repeated dummy indices, with Latin indices ranging in $\{1, 2, 3\}$ while Greek indices in $\{1, 2\}$. Accordingly, $\mathsf{C} = \mathsf{F}^T\mathsf{F}$ is the metric tensor on $\mathcal{M}$. Let us also define the stretches along the threads as $\lambda_\alpha = \sqrt{\mathsf{C}\mathbf{E}_i \cdot \mathbf{E}_i}$ and the shear deformation $\gamma = \sqrt{\mathsf{C}\mathbf{E}_1 \cdot \mathbf{E}_2/(\lambda_1\lambda_2)}$.

We account for an elastic response through the definition of an elastic free energy. Hence, we define on $\mathscr{T}$ a free energy density $W = W(\mathsf{C}, \mathsf{V}, \mathsf{W})$ per unit reference area so that the energy $\mathcal{E}_\mathcal{P}$ in the bounded part $\mathcal{P} \subset \mathscr{T}$ is given by

$$\mathcal{E}_\mathcal{P} = \int_\mathcal{P} W(\mathsf{C}, \mathsf{V}, \mathsf{W})$$

Finally, the target surface is supposed to exert no friction, except at its boundary $\partial\mathcal{N}$ where the textile is pinned. In mathematical terms, the pinning assumption translates into Dirichlet boundary conditions for the deformation $\mathbf{f}$, namely, $\mathbf{f} = \bar{\mathbf{f}}$ on $\partial\mathcal{M}$. Accordingly, the reaction forces acting on the fabric are everywhere normal to the target surface, except on its boundary.

2.2 Optimal shape control of the patch

Upon stretching a fabric, there are infinitely many patches that, once pinned on $\partial\mathcal{M}$, can be used to cover a target surface. Our goal is to search for the optimal *shape* and *pinning* of the patch, in the sense that they minimize a given cost functional $\mathscr{C}$. Thus, we aim at solving the following minimum problem

$$\min_{\mathcal{M},\bar{\mathbf{f}}} \mathscr{C}(\mathcal{M}, \mathbf{f}_{\mathcal{M},\bar{\mathbf{f}}}) \,, \tag{1}$$

where $\mathbf{f}_{\mathcal{M},\bar{\mathbf{f}}}$ is the elastic deformation ensuing from the placement of the patch onto the target surface. We remark that, since the target surface $\mathcal{N}$ is frictionless, only conservative forces act on the system and hence the mechanical equilibrium is simply obtained by elastic energy minimization. Consequently $\mathbf{f}_{\mathcal{M},\bar{\mathbf{f}}}$ is computed as

$$\mathbf{f}_{\mathcal{M},\bar{\mathbf{f}}} = \operatorname*{argmin}_{\mathbf{f}} \mathcal{E}_\mathcal{M}(\mathbf{f}) \text{ s.t. } \mathbf{f}(\mathcal{M}) = \mathcal{N},\ \mathbf{f} = \bar{\mathbf{f}} \text{ on } \partial\mathcal{M} \,. \tag{2}$$

Depending on the stretch of the fibers, the fabric can deform in three different manners [29]. If both λ_1 and λ_2 are larger than one, textile fibres are locally extended and the textile is said to be *elongated*. On the contrary, *half-slack* and *slack* configurations are obtained when one or both fibre stretches are less than unity, respectively. The last two cases arise since it is commonly assumed that textile fibres are not capable of sustaining compressive forces without buckling and wrinkling. To avoid this undesired circumstance, the optimal $\mathcal{M}$ must be searched among those patches ensuring only elongated configurations, namely

$$\lambda_i \geq 1, \quad i = 1, 2\,. \tag{3}$$

In addition, notice that the shear deformation γ equals the cosine of the angle between the fibres of the deformed textile. Therefore, by definition, $-1 \leq \gamma \leq 1$. The case $\gamma = 0$ identifies the condition whereby the two families of fibres remain orthogonal after deformation. On the contrary, initial mutually-orthogonal fibres become parallel in correspondence of the bounds $\gamma = \pm 1$. Such a limit condition identifies a singular configuration where the two fibres collapse onto one line and, due to the vanishing of areal deformation $\sqrt{\det \mathsf{C}}$, the textile fails to locally cover the target surface. Moreover, it has been observed that large shear angles can lead to wrinkling phenomena known as *shear locking* [50]. Therefore, the optimal patch must be chosen so that the shear angle is bounded, namely

$$|\gamma| \leq \gamma_{\max} < 1\,. \tag{4}$$

Finally, it is important to remark that the target shape condition corresponds to a bilateral constraint, preventing a textile from both penetrating the target surface and detaching from it. However, a unilateral constraint is closer to the physical reality, ensuring reaction forces whose normal component τ has a positive sign. Thus, the optimal patch must is searched among those satisfying the additional constraint

$$\tau \geq 0, \tag{5}$$

which we will refer to as the *unilateral obstacle condition*.

The goal of the following sections is to precisely formalize and numerically solve the *optimal clothing problem* given by Eq. (1) together with the constraints expressed by the equations (2), (3), (4) and (5).

3 Mathematical Model

3.1 Geometric setting

In the following, we assume that both $\mathcal{M}$ and $\mathcal{N}$ are smooth closed surfaces with non empty boundaries $\partial\mathcal{M}$ and $\partial\mathcal{N}$, respectively. The latter are assumed to be piece-wise regular. In order to simplify the analysis, we restrict ourselves to the case where both $\mathcal{M}$ and $\mathcal{N}$ feature a disk topology, being described by a single chart. As illustrated in the commutative diagram of Fig. 2, we parameterize both $\mathcal{M}$ and $\mathcal{N}$ in the same parameter space $\mathcal{U}$, by means of two smooth invertible functions $\boldsymbol{\psi} : \mathcal{U} \subset \mathbb{R}^2 \to \mathscr{T}$ and $\boldsymbol{\varphi} : \mathcal{U} \subset \mathbb{R}^2 \to \mathbb{E}^3$, respectively. Symbol $\boldsymbol{\theta} = (\theta_1, \theta_2)$ refers to the curvilinear coordinates of the parameter space $\mathcal{U}$ and $\nabla_{\boldsymbol{\theta}}$ denotes the gradient with respect to $\boldsymbol{\theta}$.

Since we are interested in determining the *shape* of the undeformed textile patch, we treat the function $\boldsymbol{\psi}$ as the unknown of the problem. At the same time, the parametrization $\boldsymbol{\varphi}$ is fixed and hence the *deformation map* $\mathbf{f}$ is entirely determined by $\boldsymbol{\psi}$ (see Fig. 2). Accordingly, $\mathbf{f}$ can be conveniently rewritten as

$$\mathbf{f} = \boldsymbol{\varphi} \circ \boldsymbol{\psi}^{-1}\,, \tag{6}$$

showing that our inverse deformation problem is completely ruled by the function $\boldsymbol{\psi}$.

According to Eq.(6), we can recast the surface deformation gradient in terms of the unknown $\boldsymbol{\psi}$ as follows

$$\mathsf{F} = \nabla_{\boldsymbol{\theta}} \boldsymbol{\varphi} \, (\nabla_{\boldsymbol{\theta}} \boldsymbol{\psi})^{-1}\,, \tag{7}$$

Similarly, the metric tensor $\mathsf{C} = \mathsf{F}^T\mathsf{F}$ rewrites as

$$\mathsf{C}(\boldsymbol{\psi}) = (\nabla_{\boldsymbol{\theta}} \boldsymbol{\psi})^{-T} \mathsf{a} (\nabla_{\boldsymbol{\theta}} \boldsymbol{\psi})^{-1}\,, \tag{8}$$

where $\mathsf{a} = \nabla_{\boldsymbol{\theta}} \boldsymbol{\varphi}^T \nabla_{\boldsymbol{\theta}} \boldsymbol{\varphi}$ is the first fundamental form of the target surface $\mathcal{N}$. The local change in area between the reference and deformed textile is measured by the scalar quantity $J = \sqrt{\det \mathsf{C}}$. Finally, $J_{\boldsymbol{\psi}} = \det \nabla_{\boldsymbol{\theta}} \boldsymbol{\psi}$ denotes the Jacobian of the unknown $\boldsymbol{\psi}$.

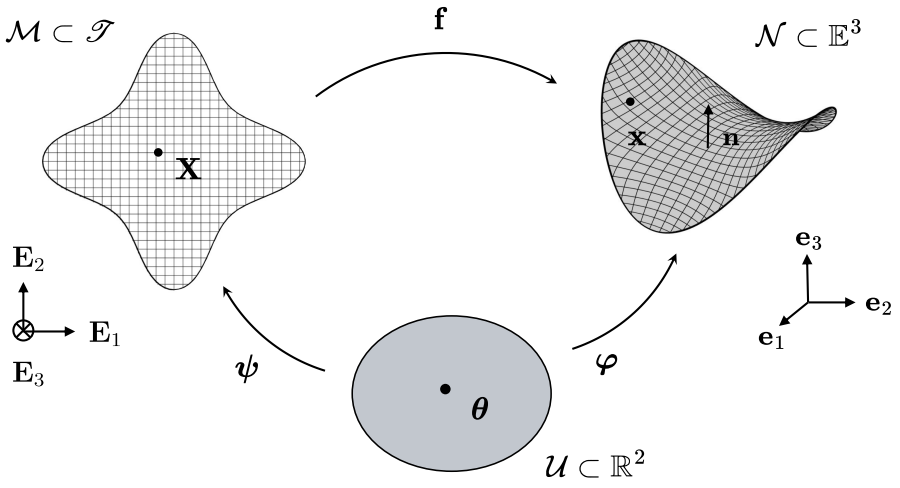

Figure 2: Commutative diagram relating the parameter set $\mathcal{U}$, the material manifold $\mathcal{M}$, and the target surface $\mathcal{N}$

3.2 Mechanical equilibrium

In-plane equilibrium As already anticipated in Eq.(2), the mechanical equilibrium of the patch can be formulated as a variational problem for the minimization of the elastic energy, namely

$$\min_{\mathbf{f} \in V_{\mathbf{f}}(\mathcal{M})} \mathcal{E}(\mathbf{f})\,. \tag{9}$$

where $V_{\mathbf{f}}(\mathcal{M}) = \{\mathbf{f} : \mathcal{M} \to \mathbb{E}^3 \,|\, \mathbf{f}(\mathcal{M}) = \mathcal{N},\, J > 0 \text{ and } \mathbf{f} = \bar{\mathbf{f}} \text{ on } \partial\mathcal{M}\}$. The definition of the set $V_{\mathbf{f}}$ includes the previously mentioned target shape condition and Dirichlet conditions on the boundary. Moreover we require J to be positive so as to guarantee the orientation preserving condition for the map $\mathbf{f}$.

To enforce mechanical equilibrium in the optimization algorithm, it is more convenient to consider the stationary condition of the problem stated in Eq.(9), as expressed by the *principle of virtual displacements*. It reads

$$\text{find } \mathbf{f} \in V_{\mathbf{f}}(\mathcal{M}) \text{ such that } \int_{\mathcal{M}} \mathsf{P} : \nabla_{\mathbf{X}} \mathbf{v} = 0 \qquad \forall \mathbf{v} \in \delta V_{\mathbf{f}}(\mathcal{M})\,, \tag{10}$$

where $\mathsf{P} = D_{\mathsf{F}} W$ denotes the first Piola-Kirchhoff stress tensor, $\mathsf{A} : \mathsf{B} := \mathrm{tr}\,(\mathsf{A}^T \mathsf{B})$ is the usual scalar product between second order tensors, and $\delta V_{\mathbf{f}}(\mathcal{M})$ represents the set of admissible variations of $\mathbf{f}$, actually the set of virtual displacement. The symbol $\nabla_{\mathbf{X}}$ denotes the gradient with respect to material coordinates X_α on the reference patch, and hence $\nabla_{\mathbf{X}} \mathbf{v} = v_{i,\alpha} \mathbf{e}_i \otimes \mathbf{E}_\alpha$.

Due to the target shape condition, only vector fields tangent to $\mathcal{N}$ are allowed inside $\delta V_{\mathbf{f}}(\mathcal{M})$. Moreover, as a consequence of the Dirichlet boundary conditions, the variations $\mathbf{v}$ must vanish on $\partial\mathcal{M}$. Hence, the space of admissible variations is defined as

$$\delta V_{\mathbf{f}}(\mathcal{M}) = \{\mathbf{v} : \mathcal{M} \to \mathbb{R}^3 \,|\, \mathbf{v}(\mathbf{X}) \in T_{\mathbf{f}(\mathbf{X})}\mathcal{N}\ \forall \mathbf{X} \in \mathring{\mathcal{M}} \text{ and } \mathbf{v} = 0 \text{ on } \partial\mathcal{M}\}, \tag{11}$$

where $T_{\mathbf{f}(\mathbf{X})}\mathcal{N}$ denotes the tangent space to $\mathcal{N}$ at the point $\mathbf{f}(\mathbf{X})$, $\mathring{\mathcal{M}}$ being the interior of the set $\mathcal{M}$.

Out-of-plane equilibrium and reaction forces Once the in-plane equilibrium is solved, we can easily recover the reaction forces $\boldsymbol{\tau}$ that the target surface exerts on the textile. This is achieved by relaxing the kinematic constraints within the space of virtual displacements and offsetting the additional degrees of freedom by adding the reactive work performed by $\boldsymbol{\tau}$. Hence, we have

$$\text{find } \boldsymbol{\tau} \text{ such that } \int_{\mathcal{M}} \mathsf{P} : \nabla_{\mathbf{X}} \mathbf{v} - \int_{\mathcal{M}} \boldsymbol{\tau} \cdot \mathbf{v} = 0 \qquad \forall \mathbf{v}\,, \tag{12}$$

where the functional spaces for $\boldsymbol{\tau}$ and $\mathbf{v}$ are left unspecified since, at least on a formal level, no special requirement is needed at this point. By testing Eq.(12) with $\mathbf{v} \in \delta V_{\mathbf{f}}(\mathcal{M})$ and exploiting Eq.(10), we immediately deduce that $\boldsymbol{\tau}$ must be of the form $\boldsymbol{\tau} = \tau\mathbf{n}$, $\mathbf{n}$ being the normal to $\mathcal{N}$ in $\mathbf{f}(\mathbf{X})$. Consequently, we can derive an equation in the unknown τ simply by testing Eq.(12) with $\mathbf{v} = v\mathbf{n}$. We finally get

$$\text{find } \tau \text{ such that } \int_{\mathcal{M}} \mathsf{P} : \nabla_{\mathbf{X}}(v\mathbf{n}) - \int_{\mathcal{M}} \tau v = 0 \qquad \forall v\,, \tag{13}$$

which allows us to compute the reaction force.

Pull-back into the space of parameters The target shape condition is enforced by writing $\mathbf{f}$ as in Eq. (6). Indeed, we recall that, through $\boldsymbol{\psi}$, we gain control over both on $\mathbf{f}$ and $\mathcal{M}$, thereby fulfilling the constraint $\mathbf{f}(\mathcal{M}) = \mathcal{N}$. However, in order to apply this change of variable, it is necessary to pull back Eq. (10) onto $\mathcal{U}$, as $\boldsymbol{\psi}$ is defined on the space of parameters. From Eqs. (7) and (8), and by means of the chain rule, we get

$$\nabla_{\mathbf{X}}\mathbf{v}|_{\boldsymbol{\psi}(\boldsymbol{\theta})} = \nabla_{\boldsymbol{\theta}}\mathbf{v}(\boldsymbol{\theta})(\nabla_{\boldsymbol{\theta}}\boldsymbol{\psi}(\boldsymbol{\theta}))^{-1}\,, \tag{14}$$

and, therefore, Eq. (10) can be formulated on $\mathcal{U}$ as

$$\text{find } \boldsymbol{\psi} \in V_{\boldsymbol{\psi}}(\mathcal{U}) \text{ such that } \int_{\mathcal{U}} J_{\boldsymbol{\psi}}\mathsf{P}(\nabla_{\boldsymbol{\theta}}\boldsymbol{\psi})^{-T} : \nabla_{\boldsymbol{\theta}}\mathbf{v} = 0 \qquad \forall \mathbf{v} \in \delta V_{\mathbf{f}}(\mathcal{U})\,. \tag{15}$$

As for the functional spaces, it trivially follows from the definition of $V_{\mathbf{f}}(\mathcal{M})$ and $\delta V_{\mathbf{f}}(\mathcal{M})$ that $V_{\boldsymbol{\psi}}(\mathcal{U}) = \{\boldsymbol{\psi} : \mathcal{U} \to \mathscr{T} \mid J_{\boldsymbol{\psi}} > 0 \text{ and } \boldsymbol{\psi} = \bar{\boldsymbol{\psi}} \text{ on } \partial\mathcal{U}\}$ and $\delta V_{\mathbf{f}}(\mathcal{U}) = \{\mathbf{v} : \mathcal{U} \to \mathbb{R}^3 \mid \mathbf{v}(\boldsymbol{\theta}) \in T_{\boldsymbol{\varphi}(\boldsymbol{\theta})}\mathcal{N}\ \forall \boldsymbol{\theta} \in \mathring{\mathcal{U}} \text{ and } \mathbf{v} = 0 \text{ on } \partial\mathcal{U}\}$. In particular, as it is evident from the definition of $\delta V_{\mathbf{f}}(\mathcal{U})$, the elements of $T_{\boldsymbol{\varphi}(\boldsymbol{\theta})}\mathcal{N}$ can be expressed solely in terms of the parametrization $\boldsymbol{\varphi}$. Specifically, $\mathbf{v}$ is an element of $\delta V_{\mathbf{f}}(\mathcal{U})$ if and only if $v_i = (\partial_{\theta_\alpha}\varphi_i)u_\alpha$ for some vector field $\mathbf{u} : \mathcal{U} \to \mathbb{R}^2$, vanishing on $\partial\mathcal{U}$. Hence, by direct application of the chain rule it follows that

$$\nabla_{\boldsymbol{\theta}}\mathbf{v} = \nabla_{\|}\mathbf{u}\,,$$

where, for the ease of notation we introduced the linear operator $\nabla_{\|}$ defined as $(\nabla_{\|}\mathbf{w})_{i\alpha} := (\partial_{\theta_\alpha}\partial_{\theta_\beta}\varphi_i)w_\beta + (\partial_{\theta_\beta}\varphi_i)(\partial_{\theta_\alpha}w_\beta)$. Finally, the variational form of the mechanical equilibrium becomes

$$\text{find } \boldsymbol{\psi} \in V_{\boldsymbol{\psi}}(\mathcal{U}) \text{ such that } \int_{\mathcal{U}} J_{\boldsymbol{\psi}}\mathsf{P}(\nabla_{\boldsymbol{\theta}}\boldsymbol{\psi})^{-T} : \nabla_{\|}\mathbf{u} = 0 \qquad \forall \mathbf{u} \in U(\mathcal{U})\,, \tag{16}$$

where $U(\mathcal{U}) = \{\mathbf{u} : \mathcal{U} \to \mathbb{R}^2 \mid \mathbf{u} = 0 \text{ on } \partial\mathcal{U}\}$.

As for Eq.(13), it can be easily pulled back onto $\mathcal{U}$ as follows

$$\text{find } \tau \text{ such that } \int_{\mathcal{U}} J_{\boldsymbol{\psi}}(\mathbb{N}[v] - \tau v) = 0 \qquad \forall v \tag{17}$$

where, for the ease of notation, we introduced the linear operator $\mathbb{N}$ defined as

$$\mathbb{N}[w] = (\mathsf{P}\nabla_{\boldsymbol{\theta}}\boldsymbol{\psi}^{-T} : \nabla_{\boldsymbol{\theta}}\mathbf{n})w + \nabla_{\boldsymbol{\theta}}\boldsymbol{\psi}^{-1}\mathsf{P}^T\mathbf{n} \cdot \nabla_{\boldsymbol{\theta}}w. \tag{18}$$

Eqs.(16,17) represent the in-plane and out-of-plane equation of mechanical equilibrium, respectively.

3.3 Constitutive law for the elastic net

In order to model the mechanical behavior of woven fabrics, we choose a strain energy density that is representative of materials with two families of fibres, i.e. warp and weft threads [51, 52]. Due to our earlier geometrical assumptions, the strain energy density is assumed to be orthotropic along the directions of the fibers, namely, $\mathbf{E}_1$ and $\mathbf{E}_2$. Moreover, we assume that only a membrane energy can be taken into account, as in most practical applications the bending stiffness of conventional textiles can be disregarded. Hence, according to [53, 54], W can be expressed as a function of the following *independent* invariants of $\mathsf{C}, \mathsf{V}, \mathsf{W}$:

$$I_1 = \mathrm{tr}\mathsf{C}\,, \qquad I_4 = \mathbf{E}_1 \cdot \mathsf{C}\mathbf{E}_1\,, \qquad I_6 = \mathbf{E}_2 \cdot \mathsf{C}\mathbf{E}_2\,, \qquad I_8 = \mathbf{E}_1 \cdot \mathsf{C}\mathbf{E}_2\,,$$

thus resulting in the general form

$$W(\mathsf{C},\mathsf{V},\mathsf{W}) = W(I_1, I_4, I_6, I_8)\,.$$

In particular, following [55] we consider an additive splitting of W as follows

$$W(\mathsf{C},\mathsf{V},\mathsf{W}) = W_1(\lambda_1) + W_2(\lambda_2) + W_S(\gamma)\,. \tag{19}$$

where, $\lambda_1 = \sqrt{I_4}$, $\lambda_2 = \sqrt{I_6}$, and $\gamma = I_8/\sqrt{I_4 I_6}$. As for the three contributions to the elastic energy, $W_1(\lambda_1)$ and $W_2(\lambda_2)$ model the energetic contributions associated with fibres extensions along $\mathbf{E}_1$ and $\mathbf{E}_2$, respectively, whereas $W_S(\gamma)$ accounts for in-plane shear elastic response.

3.4 Optimization

Since both the *shape* of $\mathcal{M}$ and the *deformation* $\mathbf{f}$ are controlled by $\boldsymbol{\psi}$, it is sufficient the adopt a cost functional depending only on $\boldsymbol{\psi}$. Specifically, we take

$$\mathscr{C}(\boldsymbol{\psi}) = \int_{\mathcal{U}} \chi(\boldsymbol{\psi})\,, \tag{20}$$

We require that the symmetries of the density χ to be a subgroup of those of the mechanical problem (see Eq.(10)). Notice that Eq.(10) is only invariant up to translations of $\boldsymbol{\psi}$, since rotations are ruled out once we fixed the orientation of the threads along $\mathbf{E}_1$ and $\mathbf{E}_2$. Hence, χ inherits those minimal symmetries, also being invariant up to translations of $\boldsymbol{\psi}$. In light of the symmetries of χ and of the equations (16),(17), (20), the optimal clothing problem can be recast as

$$\min_{\boldsymbol{\psi}\in\hat{V}_{\boldsymbol{\psi}}(\mathcal{U})} \mathscr{C}(\boldsymbol{\psi}) \quad \text{subject to:} \tag{21}$$

(i) mechanical equilibrium: $\displaystyle\int_{\mathcal{U}} J_{\boldsymbol{\psi}}\mathsf{P}(\nabla_{\boldsymbol{\theta}}\boldsymbol{\psi})^{-T} : \nabla_{\|}\mathbf{u} + \int_{\mathcal{U}} J_{\boldsymbol{\psi}}(\mathbb{N}[v] - \tau v) = 0 \qquad \forall v,\ \forall \mathbf{u}\in U(\mathcal{U}),$

(ii) elongated fiber condition: $\lambda_1(\boldsymbol{\theta}) \geq 1 \quad \text{and} \quad \lambda_2(\boldsymbol{\theta}) \geq 1, \qquad \forall \boldsymbol{\theta}\in\mathcal{U}\,,$

(iii) shear limit: $|\gamma(\boldsymbol{\theta})| \leq \gamma_{\max} \qquad \forall \boldsymbol{\theta}\in\mathcal{U}\,,$

(iv) obstacle condition: $\tau(\boldsymbol{\theta}) \geq 0 \quad \forall \boldsymbol{\theta}\in\mathcal{U}\,,$

where $\hat{V}_{\boldsymbol{\psi}}(\mathcal{U}) = \{\boldsymbol{\psi} : \mathcal{U} \to \mathscr{T}\}/V_{\text{trasl}}$, with V_{trasl} the space of translations. Taking the quotient by V_{trasl} is necessary due to the translation invariance of both $\mathscr{C}$ and the constraints. Moreover, the newly defined set $\hat{V}_{\boldsymbol{\psi}}(\mathcal{U})$ does not account either for the conditions $J_{\boldsymbol{\psi}} > 0$ or for $\boldsymbol{\psi} = \bar{\boldsymbol{\psi}}$ on $\partial\mathcal{U}$, that are instead provided in $V_{\boldsymbol{\psi}}(\mathcal{U})$. Indeed, the condition $J_{\boldsymbol{\psi}} > 0$ directly follows from the constraint (i) and (ii). In addition, we do not impose any Dirichlet conditions since we want to select the optimal pinning of the textile on the boundary. This requirement is tantamount to enlarging the set $V_{\boldsymbol{\psi}}(\mathcal{U})$ by including all the possible $\bar{\boldsymbol{\psi}}$ on $\partial\mathcal{U}$.

4 Numerical implementation

We numerically solve the optimization problem in Eq. (21) by means of a gradient descent algorithm. Different techniques are employed to handle the four constraints. Specifically, mechanical equilibrium is enforced exactly by means of Lagrange multipliers, whilst the remaining three algebraic constraints are enforced through the interior point method [56] to reduce the numerical stiffness. Thus, we search for the optimal solution as a stationary point of the following *augmented Lagrangian*

$$\begin{aligned}\mathscr{L}(\boldsymbol{\psi},\boldsymbol{\eta},\Lambda) =& \mathscr{C}(\boldsymbol{\psi}) + \int_{\mathcal{U}} J_{\boldsymbol{\psi}}\mathsf{P}(\nabla_{\boldsymbol{\theta}}\boldsymbol{\psi})^{-T} : \nabla_{\|}\boldsymbol{\eta} + \int_{\mathcal{U}} J_{\boldsymbol{\psi}}(\mathbb{N}[\Lambda] - \tau\Lambda) + \\ & \sum_{\alpha=1}^{2}\int_{\mathcal{U}} \mu_\alpha \log(\lambda_\alpha - 1) + \int_{\mathcal{U}} \mu_S \log(\gamma_{\max}^2 - \gamma^2) + \int_{\mathcal{U}} \mu_\tau \log(\tau)\,,\end{aligned} \tag{22}$$

Besides the shape map $\boldsymbol{\psi}$, symbols $\boldsymbol{\eta}$ and Λ denote the Lagrange multipliers associated to the constraint enforcing mechanical equilibrium in the tangential and transversal directions, respectively. Symbols $\mu_{1,2}$, μ_S, and μ_τ are instead tuning coefficients related to the interior point method. Their magnitude must be be set to ensure a suitable trade-off between numerical stiffness and accuracy: small values guarantee an accurate approximation of the inequality constraints but result into a stiffer problem.

Solving the nonlinear stationary conditions of $\mathscr{L}$ in a one-shot manner, by means of a Newton-Raphson method, is practically unfeasible due to the difficulty of finding suitable initial guesses for the solution ensuring convergence of the algorithm. We circumvent this difficulty by allowing $\boldsymbol{\psi}$ to evolve according to a gradient flow $\mathscr{L}$ until a steady state is attained. Specifically, in order to get a regular and smooth evolution, we solve the following $H_0^1(\mathcal{U})$-gradient flow

$$(\partial_t \boldsymbol{\psi}, \delta\boldsymbol{\psi})_{H_0^1} + D_{\boldsymbol{\psi}}\mathscr{L}[\delta\boldsymbol{\psi}] = 0 \qquad \forall \delta\boldsymbol{\psi} \in \delta\hat{V}_{\boldsymbol{\psi}}(\mathcal{U})\,, \tag{23a}$$

$$\int_{\mathcal{U}} J_{\boldsymbol{\psi}} \mathsf{P}(\nabla_{\boldsymbol{\theta}}\boldsymbol{\psi})^{-T} : \nabla_{\|}\mathbf{u} = 0 \qquad \forall \mathbf{u} \in U(\mathcal{U})\,, \tag{23b}$$

$$\int_{\mathcal{U}} J_{\boldsymbol{\psi}}(\mathbb{N}[v] - \tau v) = 0 \qquad \forall v\,. \tag{23c}$$

Here, t refers to a *pseudo*-time variable ruling the gradient flow evolution, while $(\mathbf{u},\mathbf{v})_{H_0^1(\mathcal{U})} := \int_{\mathcal{U}} \nabla_{\boldsymbol{\theta}}\mathbf{u} : \nabla_{\boldsymbol{\theta}}\mathbf{v}$ denotes the $H_0^1(\mathcal{U})$-scalar product. Notice that, since rigid-body deformations has been ruled out, $(\cdot,\cdot)_{H_0^1(\mathcal{U})}$ is indeed a scalar product.

The system of equations (23) is numerically integrated in the pseudo-time variable t using the *Backward Euler Method* while spatial discretization is performed through the Finite Element Method. The numerical implementation of the discretized problem has been carried out in a monolithic fashion using the library *FEniCS* for solving partial differential equations using Finite Element methods [57]. Specifically, we approximate $\boldsymbol{\psi}$ with second order elements, $\boldsymbol{\eta}$ and Λ with first order elements.

Finally, since we handle the unilateral constraints (ii)-(iii)-(iv) through of a logarithmic barrier, it is essential to select an initial guess $\boldsymbol{\psi}(t_0)$ that is consistent with these constraints. To this purpose, we set $\boldsymbol{\psi}(t_0)$ as a suitable reshaping of the parameter space, as detailed case by case for each numerical examples. Instead, the constraint given by mechanical equilibrium does not require a compatible initialization. It can be relaxed during the first iterations of the algorithm by replacing the gradient flow in the first centering step of the interior point method with the following saddle-point dynamics

$$(\partial_t \boldsymbol{\psi}, \delta\boldsymbol{\psi})_{H_0^1} - (\partial_t \boldsymbol{\eta}, \mathbf{v})_{H_0^1} + D_{\boldsymbol{\psi},\boldsymbol{\eta}}\mathscr{L}[\delta\boldsymbol{\psi}, \mathbf{v}] = 0 \qquad \forall \delta\boldsymbol{\psi} \in \delta\hat{V}_{\boldsymbol{\psi}}(\mathcal{U}),\ \forall \mathbf{v}\,. \tag{24}$$

Once mechanical consistency is achieved in the first centering step, then the interior point method proceeds normally as detailed in Algorithm 3.

Gradient-based optimization algorithm

Choose: $\mu = (\mu_\alpha, \mu_S, \mu_\tau)$
Set: $\boldsymbol{\psi}(t_0)$ and $\mu_0 > \mu$
`% interior point method`
`% Solve saddle point dynamics Eq.(24) until steady state, with parameters` μ_0
while $(\partial_t \mathscr{C} \geq \varepsilon)$ **do**
  Find $\boldsymbol{\psi}_{j+1}$, $\boldsymbol{\eta}_{j+1}$ s.t.
  $(\boldsymbol{\psi}_{j+1} - \boldsymbol{\psi}_j, \delta\boldsymbol{\psi})_{H_0^1(\mathcal{U})} - (\boldsymbol{\eta}_{j+1} - \boldsymbol{\eta}_j, \delta\boldsymbol{\eta})_{H_0^1(\mathcal{U})} + \Delta t D_{(\boldsymbol{\psi},\boldsymbol{\eta},\Lambda)} \mathscr{L}(\boldsymbol{\psi}_{j+1}, \boldsymbol{\eta}_{j+1})[\delta\boldsymbol{\psi}, \delta\boldsymbol{\eta}, \delta\Lambda] = 0 \quad \forall \delta\boldsymbol{\psi}, \delta\boldsymbol{\eta}, \delta\Lambda$
  $t_{j+1} = t_j + \Delta t$
end while
$\mu_1 = \mu_0/2$
$i = 1$
while $\mu_i > \mu$ **do**
  `% centering step: solve Eq.(23) until steady-state with parameters` μ_i
  while $(\partial_t \mathscr{C} \geq \varepsilon)$ **do**
    Find $\boldsymbol{\psi}_{j+1}$ s.t. $(\boldsymbol{\psi}_{j+1} - \boldsymbol{\psi}_j, \delta\boldsymbol{\psi})_{H_0^1(\mathcal{U})} + \Delta t D_{(\boldsymbol{\psi},\boldsymbol{\eta},\Lambda)} \mathscr{L}(\boldsymbol{\psi}_{j+1})[\delta\boldsymbol{\psi}, \delta\boldsymbol{\eta}, \delta\Lambda] = 0 \quad \forall \delta\boldsymbol{\psi}, \delta\boldsymbol{\eta}, \delta\Lambda$
    $t_{j+1} = t_j + \Delta t$
  end while
  choose $\mu_{i+1} = \mu_i/2$
  $i \leftarrow i + 1$
end while

Figure 3: Scheme of the implementation of the optimization algorithm. First, we select a feasible $\boldsymbol{\psi}(t_0)$ with respect to the unilateral constraints (ii)-(iii)-(iv) and choose a value for the barrier parameters μ that ensures a good trade-off between accuracy and numerical stiffness. Subsequently, we optimize $\boldsymbol{\psi}$ using Eq. (24) to additionally enforce mechanical equilibrium. Finally, we iterate through multiple centering steps gradually decreasing the barrier parameters μ_i until the optimal μ is achieved.

5 Numerical results

In this section, we illustrate the potential of the proposed optimization tool through a series of numerical examples. In particular, we consider two different target surfaces: the unit sphere (as a prototype of surface with positive Gaussian curvature) and the hemicatenoid (as a prototype of surface with negative Gaussian curvature). We parameterize the former surface using the stereographic projection, namely

$$\boldsymbol{\varphi}^{\mathrm{sph}}(\theta_1,\theta_1)=\left\{2\,r\,\frac{\theta_1}{1+r^2(\theta_1^2+\theta_2^2)}\,,\,2\,r\,\frac{\theta_2}{1+r^2(\theta_1^2+\theta_2^2)}\,,\,\frac{-1+r^2\,(\theta_1^2+\theta_2^2)}{1+(\theta_1^2+\theta_2^2)}\right\}\,,$$

with θ_1 and θ_1 belonging to the unit disk. The parameter r is a positive constant that quantifies the amount of spherical surface to be clothed: $r=1$ corresponds to the clothing of a hemisphere, while the whole sphere is obtained for $r\to\infty$. The hemicatenoid is instead described by the explicit parametrization

$$\boldsymbol{\varphi}^{\mathrm{cat}}(\theta_1,\theta_1)=\{\cosh\theta_2\cos\theta_1,\cosh\theta_2\sin\theta_1,\theta_2\}\,,$$

where $(\theta_1,\theta_2)\in(0,\pi)\times(-1,1)$.

In all the examples that follow, we assume that the strain-energy density has the following expression

$$W(\mathsf{C})=K_c\,(I_4-1)^2+K_c\,(I_6-1)^2+K_S I_8^2\,, \tag{25}$$

where parameters k_c and k_s refer to the threads and shear stiffness, respectively. This constitutive choice ensure that the orthotropic strain energy function is polyconvex [58], thus an elastic solution exists.

Moreover, we take as cost functional the elastic energy itself, namely

$$\mathcal{C}(\boldsymbol{\psi})=\int_{\mathcal{M}}W(\mathsf{C}(\boldsymbol{\psi}))\,. \tag{26}$$

For what concerns the barrier coefficients involved in the interior point method, all the simulations have been finally performed by setting $\mu_0=10$ and $\mu_\alpha=\mu_S=\mu_\tau=0.001$.

5.1 Clothing with Chebyshev nets

We first benchmark the proposed optimization algorithm against some known results in the Chebyshev net theory. According to [25, 59], it is indeed possible to clothe the unit-hemisphere avoiding any geometric singularity using a Chebyshev net, i.e. an ideal fabric made of inextensible threads and negligible shear resistance. Consequently, Chebyshev nets have zero elastic energy and then represent a global minimum of $\mathcal{C}$. Hence, the benchmark consists in verifying that, our optimization procedure using $k_s=0$ results into a Chebyshev net.

We can take advantage of the existence of such nets and facilitate the initialization of the algorithm by getting rid of all the inequality constraints.

Figure 4a shows the shape of the optimal patch covering the hemisphere compared against the one obtained through the procedure illustrated in [59], relying on the Chebyshev net theory. We remark that, there are generally many Chebyshev nets covering a given target surface. In order to obtain a specific solution, it is necessary to impose additional conditions to the optimization problem. For this purpose, the following results are obtained by requiring the patch to be symmetric with respect to the vertical and horizontal axes.

From this comparison, it turns out that the optimization indeed converges toward a Chebyshev net as, predicted, since the curves reported in Fig. 4a are practically identical. In Fig. 4b we represent the patch in its deformed configuration once it has been placed onto the target surface. Because of the inextensibility of the threads, the textile exhibits only shear deformations by changing the angle between the initially orthogonal threads. More precisely, the spatial distribution of the shear γ is plotted in Fig. 5a. We find that γ vanishes along the axes of symmetry of the patch, where the deformed fibres remains mutually orthogonal. Conversely, the shear angle undergoes significant variations along the diagonal directions, ensuring that the fabric conforms effectively to the target surface. In Fig. 5b we plot the profile of γ along the line ab, drawn on the undeformed patch. Even in this case, the outcomes of the optimization procedure are in perfect

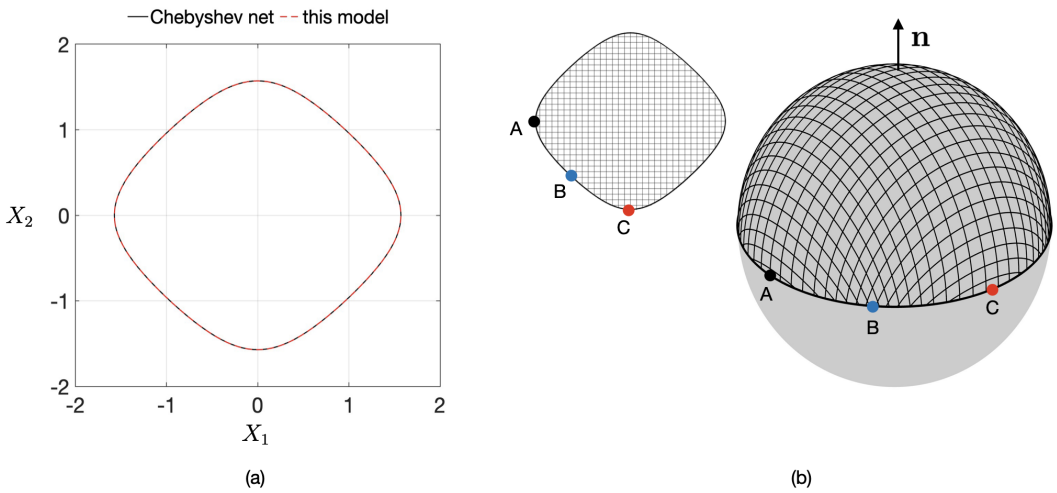

Figure 4: Clothing a unit-hemisphere with a Chebyshev net. (a) Resulting optimal patch shape compared to the one obtained from the theoretical Chebyshev net solution. (b) Deformed shape of the optimal textile patch onto the target surface. A regular array of mutually orthogonal threads have been sketched on the fabric patch (top left) to mark fabric deformation (right). For the initial condition we set $\psi(0) = \{0.5\,\theta_1, 0.5\,\theta_2\}$.

agreement with the Chebyshev net theory, by which the shear deformation yields the following asymptotic expression [59]

$$\gamma(s) \simeq \cos\left(\frac{\pi}{2} - \frac{s^2}{2} + \frac{s^6}{144}\right), \tag{27}$$

s being the arc-length of line ab.

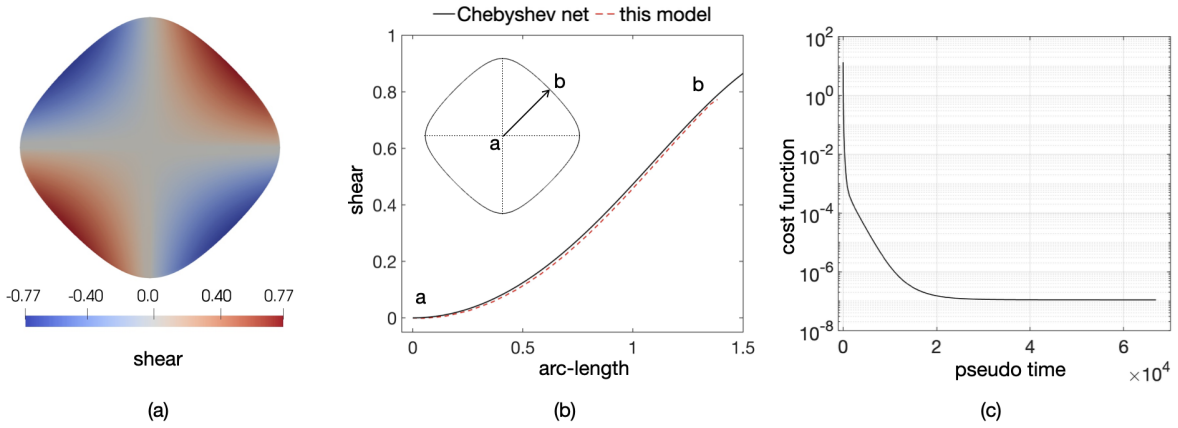

Figure 5: Clothing a unit-hemisphere with a Chebyshev net. (a) Spatial distribution of the shear angle γ *for the optimal patch shape. (b) Plot of the shear deformation* γ *along the reference line ab and comparison with the Chebyshev net model Eq. (27). (c) Evolution of the non-dimensional cost function of* $\mathcal{C}/(2\pi k_c)$ *versus the pseudo-time.*

In Fig. 5c we report the decay of the cost function $\mathcal{C}$ along the gradient flow to illustrate the performance of the optimization algorithm. Large values of the cost function are obtained at first, since high values of thread stretches are required to deform the fabric onto the surface. Subsequently, the algorithm modifies the shape of the textile patch to release the fibre elongation. The optimal solution is eventually attained for a non-dimensional strain energy of approximately 1×10^{-7}, where both λ_1 and λ_2 are equal to 1 everywhere. A similar result is found for clothing the hemicatenoid with a Chebyshev net. In Fig. 6 we report the resulting

optimal shape of the patch along with its corresponding deformed shape, together with the distribution of the shear angle.

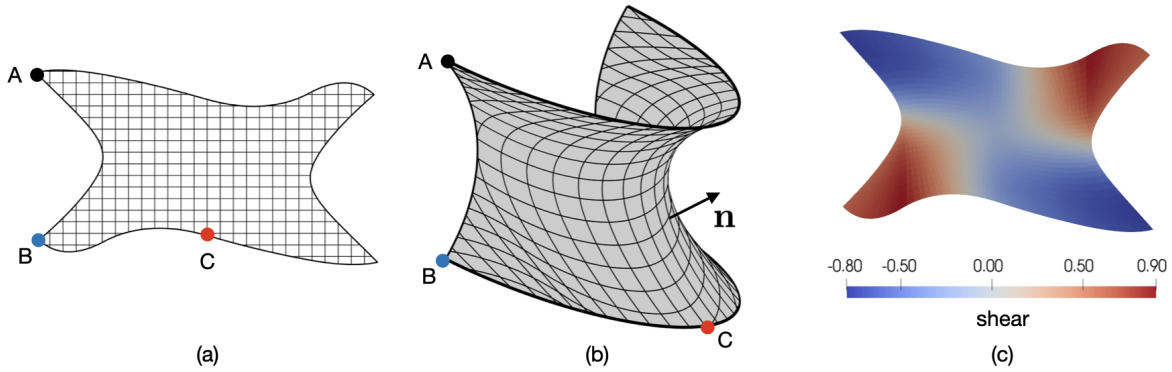

Figure 6: Clothing the hemicatenoid with a Chebyshev net. (a) Resulting optimal patch shape for vanishing shear rigidity. (b) Deformed shape of the optimal textile patch onto the target surface. (c) Spatial distribution of the shear angle γ for the optimal patch shape. For the initial condition we set $\boldsymbol{\psi}(0) = \{0.5\,\theta_1, 0.5\,\theta_2\}$.

5.2 Clothing with elastic fabrics

In the previous section we considered the limit of Chebyshev nets as $k_s/k_c \to 0$. In this scenario, the deformed configuration is solely driven by the geometrical properties of the target surface $\mathcal{N}$: elasticity ceases to be a factor, as the strain energy vanishes and elastic forces no longer influence the structure.

In this section, we tackle the more general problem of finding optimal covering patches with elastic fabrics. We will refer to them as *optimal elastic patches*. For the model at hand, they arise when non-developable surfaces are clothed with fabrics having non vanishing shear and threads rigidity. Alternatively, they can also emerge when the shear deformation γ is constrained by an upper limit.

Besides ensuring mechanical equilibrium, our numerical simulation take into account for the constraints enforcing the tensile condition of the threads and the shear limit. We remark that, at this stage, the shear bound is implemented solely to prevent singular configurations from appearing along the optimization path by taking $\gamma_{\max} = 0.95$. In practice, the optimal solution displays shear deformations well below the upper limit $\gamma_{\max}$ which then does not affect the shape of the patch. For the sake of clarity, we first disregard the constraint acting on the reaction force τ, that will be considered in a later step.

In figures 7a and 8a we plot the shape of optimal elastic patches for different values of k_s/k_c for the cases of the hemisphere and the hemicatenoid, respectively. Such solutions are depicted against the corresponding Chebyshev net patch (i.e. $k_s = 0$) to illustrate the effect of the shear rigidity of the fabric on the resulting patch shape. The optimal patch clothing the hemisphere shrinks as the ratio k_s/k_c increases. Moreover, the solution gradually displays a morphological transition from a diamond shape to a squared one. This behavior is clearly driven by the interplay between the threads stiffness and shear rigidity. In Fig. 7b we plot the deformed patch for the case $k_s/k_c = 100$. By comparing it with Fig. 4b, we see that a higher shear rigidity promotes smaller shear deformations at the expense of greater fiber stretches. The elongation of the threads becomes apparent when comparing the dimension of the fabric's unit cell in the two cases. This is also apparent in Figs. 7c-d, illustrating the fiber stretch λ_1 and shear angle γ for the hemisphere with $k_s/k_c = 100$. We readily see that most of the stretch occurs in the interior of the patch with a maximum of a 80% elongation of the threads (identical considerations hold for λ_2 by spherical symmetry). Conversely, γ is everywhere very low with extreme values of about ± 0.075. Therefore, orthogonality between fibres is practically preserved in the deformed fabric.

A significant shape change with respect to variations of the the ratio k_s/k_c is also observed for the hemicatenoid, as depicted in Fig. 8a. In particular, the area of the patch decreases as we increase the shear rigidity, and an orthotropic symmetry along the vertical and horizontal axes is gradually established. Similar considerations to the ones reported for the unit-hemisphere hold concerning the interplay between shear rigidity and thread stiffness. However, the elongation of the fibers localizes in this case close to the patch boundaries. Such a difference is correlated with the opposite sign of the Gaussian curvature, which

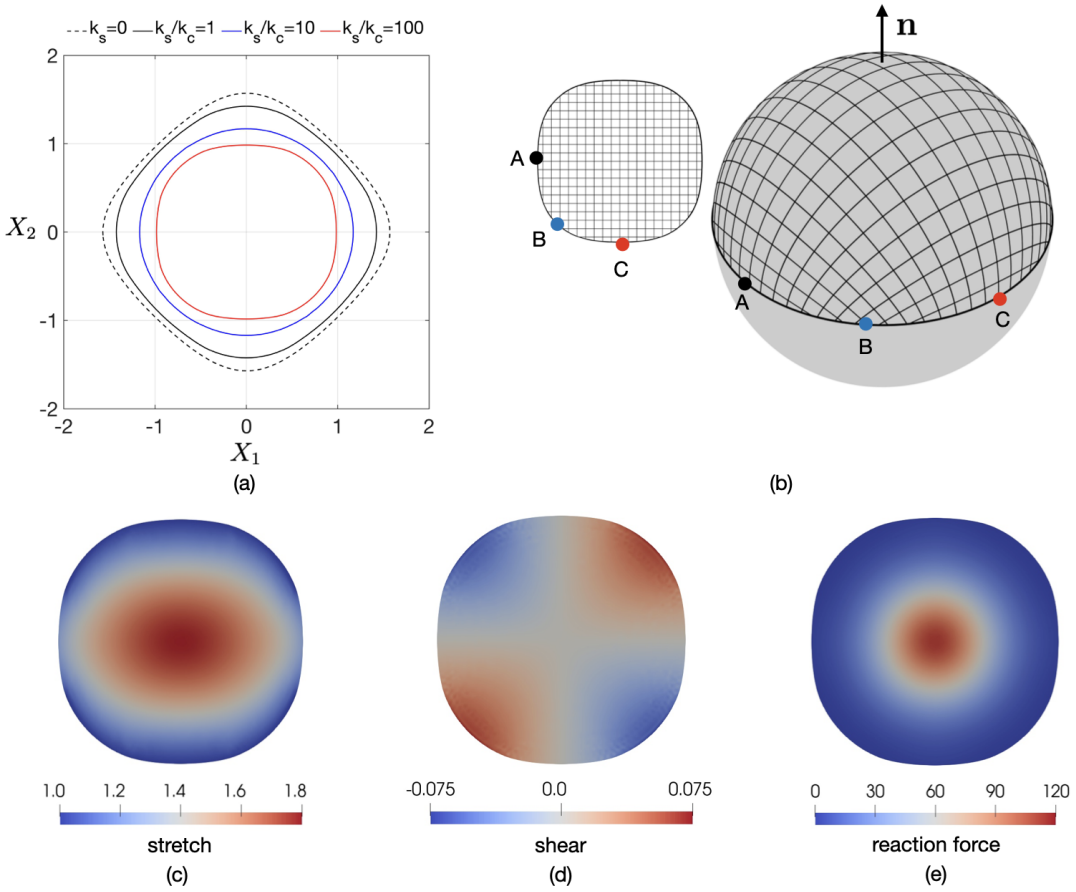

Figure 7: Clothing the unit-hemisphere with an elastic fabric. (a) Optimal patch shape resulting for different values of the ratio k_s/k_c. (b) Deformed shape of the optimal textile patch onto the target surface in the case of $k_s/k_c = 100$. (c)-(d)-(e) Spatial distribution of the resulting stretch λ_1, shear angle γ, and non-dimensional normal reaction force τ/k_c in the case of $k_s/k_c = 100$. For the initial condition we set $\boldsymbol{\psi}(0) = \{0.5\,\theta_1, 0.5\,\theta_2\}$.

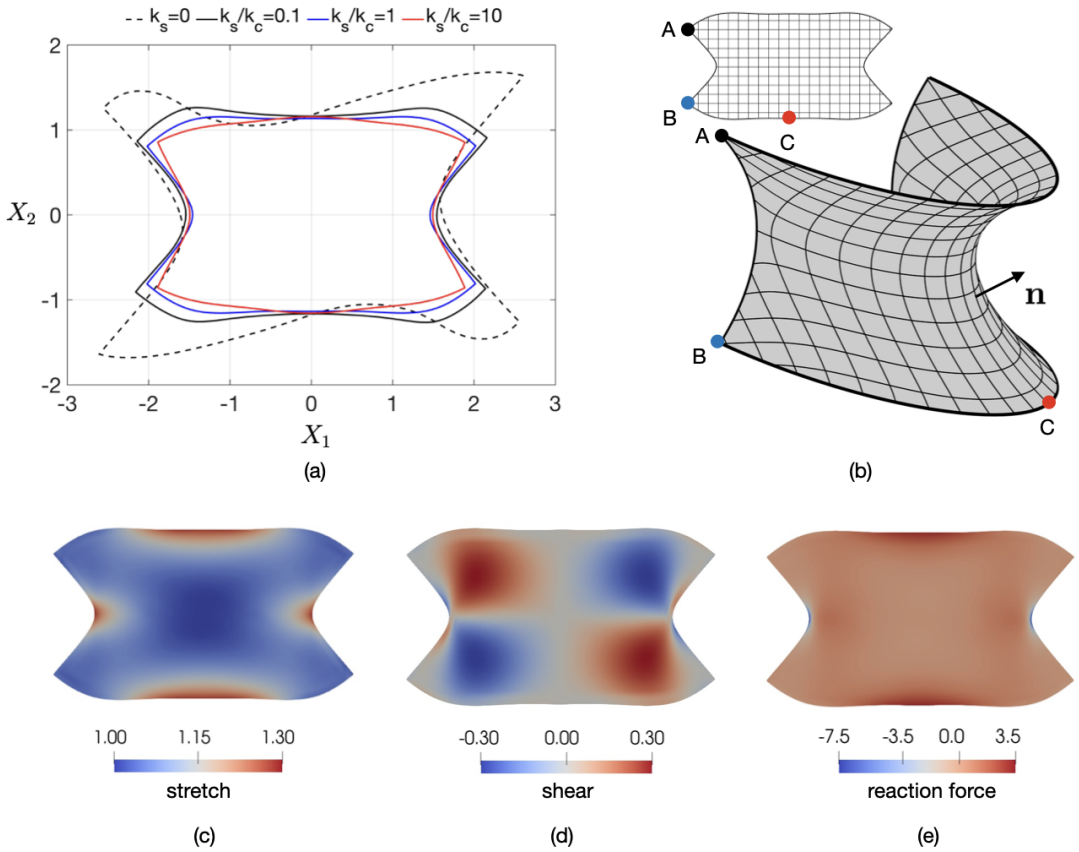

Figure 8: Clothing the hemicatenoid with an elastic fabric. (a) Optimal patch shape resulting for different values of the ratio k_s/k_c. (b) Deformed shape of the optimal textile patch onto the target surface in the case of $k_s/k_c = 1$. (c)-(d)-(e) Spatial distribution of the resulting stretch λ_1, shear angle γ, and non-dimensional normal reaction force τ/k_c in the case of $k_s/k_c = 1$. For the initial condition we set $\boldsymbol{\psi}(0) = \{0.5\,\theta_1, 0.5\,\theta_2\}$.

imposes a greater fiber stretch to accommodate the local metric of the target surface in proximity to the boundaries.

We further focus on the analysis of the reaction force exerted by the target surface. In Figs. 7e and 8e, we plot the spatial distribution of τ/k_c for the hemisphere and the hemicatenoid, respectively. In the former case, τ is everywhere non-negative and attains its maximum value in the center of the patch. Hence, the obstacle condition is everywhere satisfied. Conversely, the obstacle condition is violated in the case of the hemicatenoid since τ attains both positive and negative values. The enforcement of the unilateral obstacle condition in this context will be discussed in a dedicated section.

Finally, we depict in Fig. 9 a convergence plot of the optimization algorithm. The Lagrangian objective function $\mathcal{L}$ exhibits a staircase profile where the jumps in Fig. 9a corresponds to the initiation of each centering step of the interior point method. In fact, the contributions associated to the barriers change significantly at each iteration of the parameter μ. The jumps are more pronounced at the beginning of the simulation, as the absolute variation of μ is bigger. In addition, the objective function attains negative values in the first iteration of the interior point method (i.e. $\mu = 10$). This happens because the barrier function is the dominant energetic contribution in the first stages, as shown in Fig. 9b. As the optimization proceeds, the magnitude of the barrier function progressively decreases, eventually becoming negligible compared to the cost function. For completeness, Fig. 9b also details the profile of the cost function showing the convergence toward a local minimum.

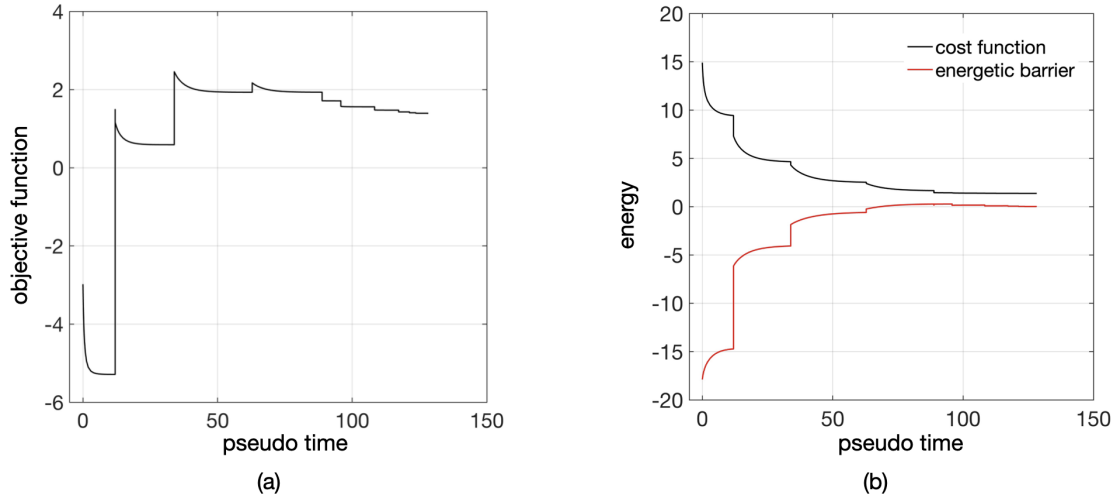

Figure 9: Convergence of the optimization algorithm based on the interior point method. (a) Plot of the non-dimensional objective function $\mathcal{L}/(2\pi k_c)$ against pseudo-time. (b) Plot of the non-dimensional cost function and non-dimensional barrier function against pseudo time. Both the reported results refer to the hemispherical surface in the case $k_s/k_c = 100$.

5.3 Clothing large portions of a sphere

It is worth remarking that the problem of finding a Chebyshev net may not always have a solution, even for target surfaces topologically equivalent to a disk [60, 61, 62, 63]. Indeed, the presence of singularities resulting from localized fiber collapse (i.e. $\gamma = \pm 1$) hinders the existence of a global solution. For instance, covering large portions of the unit sphere leads to the formation of a locus of singularities that, in the (X_1, X_2) plane, approximates the hyperbola $X_2 \simeq \pm 1.86/X_1$ [26].

Geometric singularities can be properly detected by our optimization procedure as illustrated in Fig. 10, where we plot the shape of Chebyshev net patches covering different portions p of the unit-sphere. We find that increasing p does not significantly alter the shape of the patch with respect to the one obtained for the hemisphere. The locus of singularities is delineated by a dashed line Fig. 10a, revealing that singular solutions appear beyond a portion threshold $p \approx 85\%$. This fact is also confirmed by Fig. 10b, showing the maximum value of the shear angle for different values of p. In Fig. 10c-e we plot both the deformed

and undeformed configurations of a Chebyshev net covering 85% of the sphere. In particular, in Fig. 10c-d, we can appreciate four geometric singularities localized on the boundary of the patch, where warp and weft threads locally collapse onto the same line.

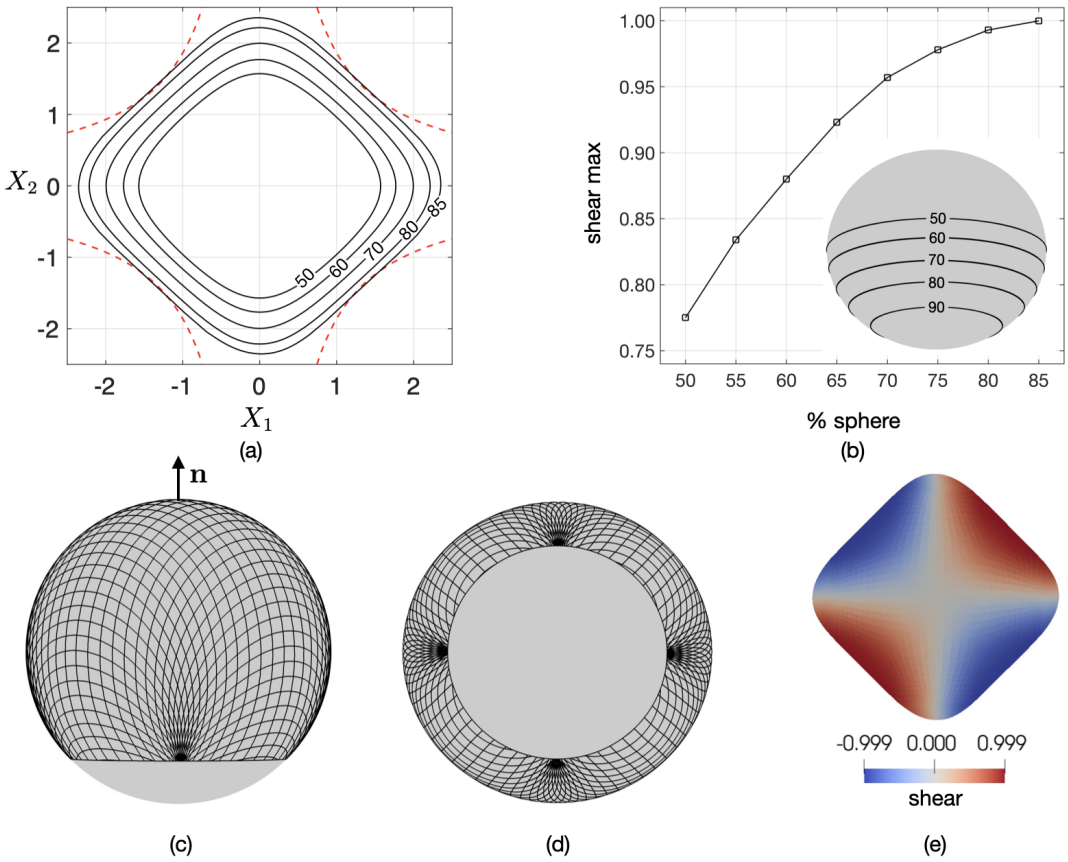

Figure 10: Clothing large portions of the unit-sphere with a Chebyshev net. (a) Plot of the patch shapes obtained for increasing percentage of the covering spherical area. (b) Evolution of the simulated maximum shear angle for the considered covering patches. (c-d-e) Shape of problem singularities and spatial distribution of the shear angle for a Chebyshev net covering 85% of a unit-sphere. For the initial condition we set $\psi(0) = \{0.1\,\theta_1, 0.1\,\theta_2\}$ *in all the considered cases.*

The emergence of singularities hinders the fabrication of single-piece covering nets. A common strategy to avoid fiber collapse consists in covering the target surface with multiple patches sewn together. Cut or sewn lines can be designed with the aid of optimization procedures as proposed by [44]. Here, we propose a new strategy to avoid such singularities in single-patch covering by means of elastic fibers. In the context of our optimization problem this can be achieved by enforcing an upper bound for $|\gamma|$, as shown in Fig. 11. We perform the simulations considering a fabric with vanishing shear rigidity and set the upper bound for γ at $\gamma_{\max} = \cos \pi/6)$. For $p < 60\%$, the shear never exceeds $\gamma_{\max}$ and so the optimal elastic patch is the one obtained for Chebyshev nets (compare Fig. 11a with Fig. 10a). Instead, a significant shape change occurs when $p > 60\%$, as the unilateral shear constraint becomes active. Moreover, the area of the undeformed patches does not monotonically increase with p. Specifically, the larger patch is obtained for $p \approx 85\%$. Indeed, covering larger areas under the shear constraint, requires a higher thread elongation, which causes a significant areal reduction of the patch (compare the patch shapes for $p = 80\%$ and $p = 90\%$ in Fig. 11a). In Figs. 10b-c, we represent the deformed state of an elastic fiber net covering 85% of the sphere: differently from the Chebyshev net in 10c-d, there are no geometric singularities. Furthermore, it is worth noting that for high values of p, the optimal patch exhibits a singular boundary with four corners. This intriguing observation suggests that fiber elasticity may eliminate the net's singularities and may trigger singular features in the shape of the patch (compare Fig. 10e with Fig. 11e). Finally, we present stretch

and stress states of the resulting fabric in Figs. 11d-f.

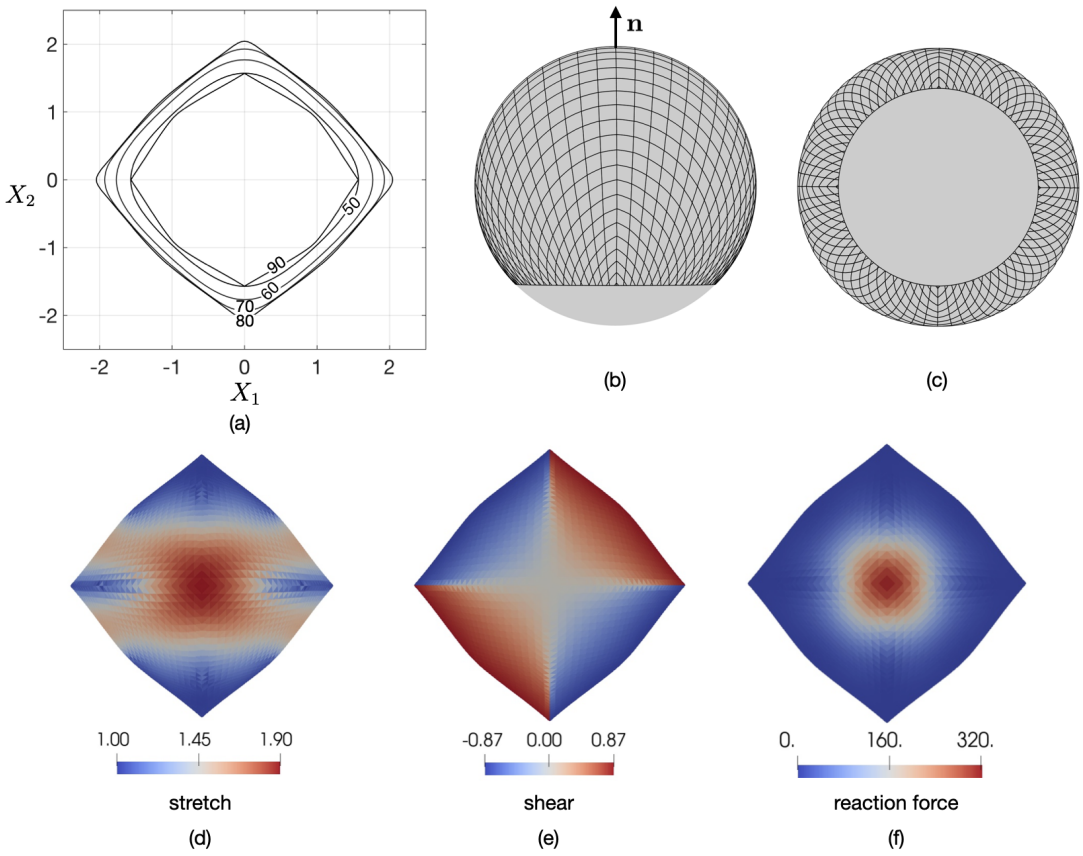

Figure 11: Clothing large portions of a unit-sphere with an elastic net ($k_s = 0$). (a) Plot of the patch shapes obtained for increasing percentage of the covering spherical area. (b-c) Side and bottom views of the elastic net covering 85% of the unit-sphere. (d-e-f) Spatial distribution of the fabric stretch λ_1, shear angle γ, and dimensionless reaction force τ/k_c for an elastic net covering 85% of a unit-sphere. For the initial condition we set $\boldsymbol{\psi}(0) = \{0.1\,\theta_1, 0.1\,\theta_2\}$ in all the considered cases.

5.4 Application of the unilateral obstacle condition

Among the examples detailed in Sec.5.2, only some of them display a spatial distribution of the normal reaction force τ consistent with the unilateral obstacle condition (i.e. $\tau \geq 0$). In particular, in the case of the hemicatenoid, τ assumes both positive and negative values. To address this issue, we performed additional numerical simulations for the hemicatenoid under the same conditions adopted in Sec. 5.2, while enforcing the unilateral constraint $\tau \geq 0$. We remark that the initial guess for the solution must now be compatible with the obstacle condition as well. This is in general a non trivial task that must handled carefully in order to ensure numerical convergence.

In Fig. 12 we compare the shapes of the patches with and without enforcing the unilateral obstacle condition, for low ($k_s/k_c = 1$) and high ($k_s/k_c = 100$) values of the relative shear stiffness. For $k_s/k_c = 1$, the two shapes exhibit only minor differences whereas higher ratios lead to great shape variations. The latter are primarily achieved through a rotation of the patch, which breaks the orthotropic symmetry of the problem (see Fig. 12c-d). Such a difference might be attributed to the different distribution of the reaction force shown in Figs. 12a-b. Indeed, the region with incompatible reaction forces ($\tau < 0$) is much smaller for low shear stiffness and is primarily restricted to the lateral part of the patch. Not surprisingly, the magnitude of relative rotation continuously increases with the rise of the shear stiffness, as reported in Fig. 13. There we represent the optimal patch shape constrained with $\tau \geq 0$ for increasing values of k_s/k_c.

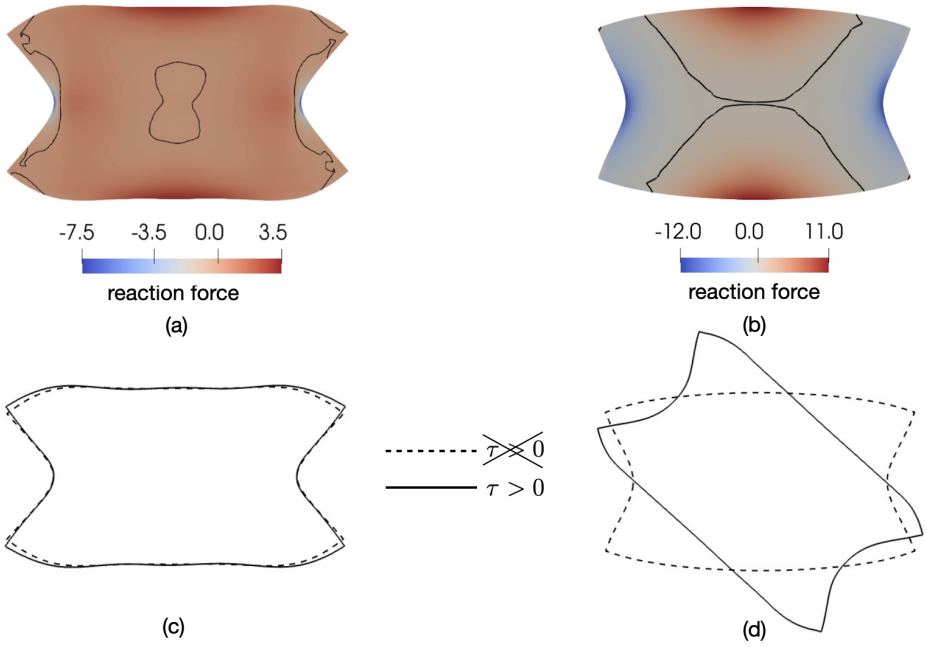

Figure 12: Resulting normal reaction force τ/k_c for the target hemicatenoid without the unilateral obstacle condition for (a) $k_s/k_c = 1$ and (b) $k_s/k_c = 100$. The superposed black curves mark locus of points with $\tau = 0$. (c-d) Comparison between optimal patch shapes with and without the unilateral obstacle condition $\tau > 0$ for $k_s/k_c = 1$ and $k_s/k_c = 100$, respectively. For the initial condition we set $\boldsymbol{\psi}(0) = \{0.3\,\theta_1, 0.4\,\theta_2\}$.

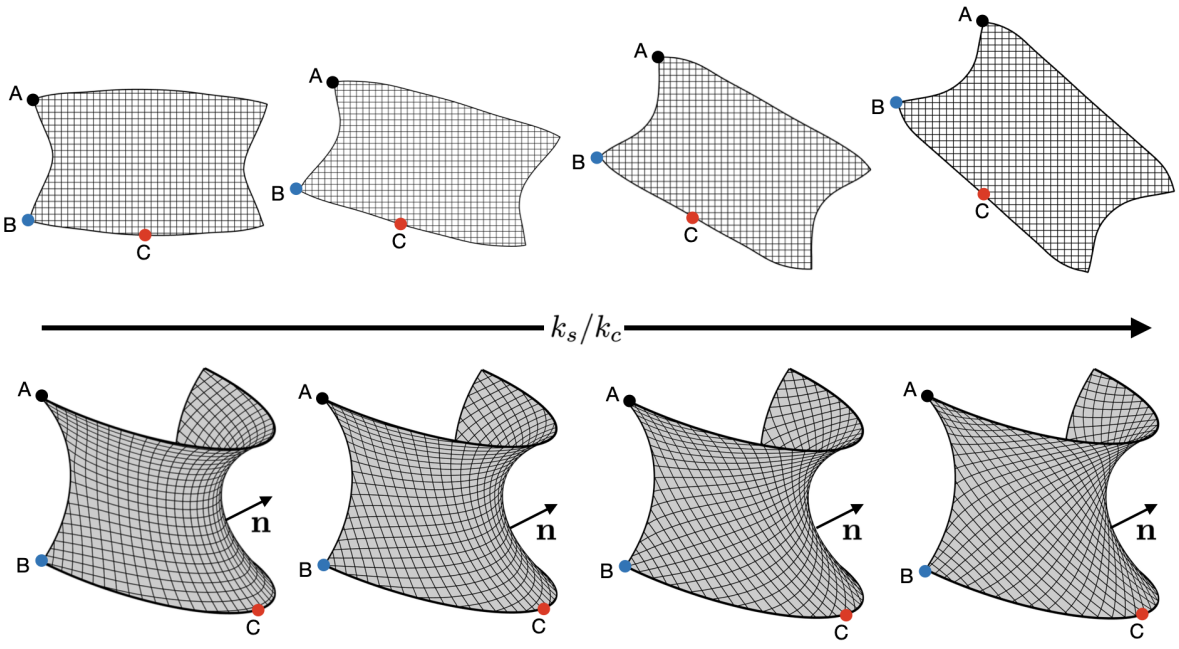

Figure 13: (Top) Simulated optimal patch shapes for the target hemicatenoid shown at increasing relative shear stiffness k_s/k_c (i.e. k_s/k_c = 70, 80, 90, 100) along with the obstacle condition $\tau \geq 0$. (Bottom) Correspondent shape of the deformed textile for the reported optimal patches with the black arrow indicating the surface normal $\mathbf{n}$. For the initial condition we set $\boldsymbol{\psi}(0) = \{0.3\,\theta_1, 0.4\,\theta_2\}$ for all the considered cases.

6 Discussion and conclusions

This work proposed a novel optimization tool for designing elastic cloths covering a given target surface. In order to solve the corresponding inverse design problem, we proposed an optimal control method to identify the initial cloth shape for covering a smooth and rigid surface, minimizing a given a cost functional. We formulated a constrained optimization problem that is numerically solved using a constrained gradient descent algorithm. In the test cases under consideration, the cost function is related to the elastic energy of the textile, that is considered here as a single-patch, anisotropic membrane. The target surface is frictionless, except at its boundary where the textile is pinned, imposing a unilateral obstacle condition for the reactive forces at the target surface. The constrained optimization problem also accounts for an elongation condition of the warp and weft fibers, possibly with bounded shearing angle.

First, we validated our numerical tool by bench-marking the numerical outcomes against the known theoretical results for Chebyshev net on a unit hemisphere, obtaining an excellent agreement. Second, we investigated the effect of the fabric elastic properties on the shape of the cloth. Beyond the state-of-the-art, we showed how geometric singularities, emerging in the Chebyshev net covering a large portion of a unit sphere, can be avoided whence considering fiber elongation. Remarkably, the optimal elastic patch for an elastic net covering a sphere develops an edgy shape endowed with four corners that are exactly placed where the singularities have been removed. Although heuristic, this observation seems to suggest that fiber net elasticity allow to transfer singularities in the network into singularities in the shape of the patch.

We also investigated the optimal shapes optimal elastic patches for the cases of the hemisphere and the hemicatenoid at different values of k_s/k_c. In both cases, we obtain characteristic morphological transitions of the elastic patch, whose area shrinks as the shear rigidity is increased with respect to the fiber stiffness, as surface stretching is preferred to shearing. The effect of the different Gaussian curvature is evident in the spatial distribution of the local stretch, localising at the core of the patch for the hemisphere and at the patch boundary for the hemicatenoid. Finally, we analyzed the spatial distribution of the normal reaction forces τ that the surface exerts on the fabric. In particular, we showed that for the hemicatenoid, the orthotropic symmetry of the patch is broken when considering the unilateral obstacle constraint.

This work proposed a novel optimization method for the inverse design of elastic clothes that is limited by a few geometric and constitutive assumptions. Further developments of the model will focus on including out-of-plane constitutive responses typical of nonlinear elastic shells [64], e.g. fabric bending. Non-local effects can also be captured by considering higher-order deformation measures [52]. This choice would allow a more accurate simulation of the mesoscopic structure of the textile. Moreover the smoothing effect of the strain gradient in the free energy could possibly enhance the performance of the optimization algorithm and ease the numerical solution the mechanical problem. It would be also interesting to integrate the proposed elastic approach into the geometric framework adopted in [44]. This choice would allow us to widen the focus from parameterized target surfaces to the processing of discrete, pointwisely defined surfaces. In addition, it will allow to explore the role of different network topologies of the elastic patch. Finally, we plan to include multi-physic couplings in the constitutive law of the fabrics, e.g. nonlinear electro-elasticity [65] or active swelling [66], to apply cloth optimization for the inverse design of smart textiles [67] and 4D printed fabrics [68].

Acknowledgments

We gratefully acknowledge partial support from MUR grants Dipartimento di Eccellenza 2023-2027 and PRIN 2020 2020F3NCPX, and from European Commission through FSE REACT-EU funds, PON Ricerca e Innovazione.

References

[1] K.M.F. Hasan, P.G. Horváth, and T. Alpár. Potential fabric-reinforced composites: a comprehensive review. *J. Mater. Sci.*, 56:14381–14415, 2021.

[2] M. Magri and P. Ciarletta. Mathematics meets the fashion industry on path to product innovation and sustainability. *Proc. R. Soc. A: Math. Phys. Eng. Sci.*, 479(2274):20220715, 2023.

[3] F. Momeni, S.M. Mehdi Hassani.N, and X. Liu. A review of 4d printing. *Mater. Des.*, 122:42–79, 2017.

[4] B. Liang and P. Boisse. A review of numerical analyses and experimental characterization methods for forming of textile reinforcements. *Chinese J. Aeronaut.*, 34(8):143–163, 2021.

[5] M. Mehrpouya, A. Azizi, S. Janbaz, and A. Gisario. Investigation on the functionality of thermoresponsive origami structures. *Adv. Eng. Mater.*, 22(8):2000296, 2020.

[6] E. Siéfert, E. Reyssat, J. Bico, and B. Roman. Programming curvilinear paths of flat inflatables. *Proc. Natl. Acad. Sci. U.S.A.*, 116(34):16692–16696, 2019.

[7] T. D. Ngo, A. Kashani, G. Imbalzano, K. Nguyen, and D. Hui. Additive manufacturing (3d printing): A review of materials, methods, applications and challenges. *Compos. B. Eng.*, 143:172–196, 2018.

[8] J.V. Beck and K.A. Woodbury. Inverse problems and parameter estimation: integration of measurements and analysis. *Meas. Sci. Technol.*, 9:893, 1998.

[9] D. Andrini, G. Noselli, and A. Lucantonio. Optimal design of planar shapes with active materials. *Proc. R. Soc. A: Math. Phys. Eng. Sci.*, 478(2266):20220256, 2022.

[10] R. Ortigosa, J. Martínez-Frutos, C. Mora-Corral, P. Pedregal, and F. Periago. Optimal control and design of magnetic field-responsive smart polymer composites. *Appl. Math. Model.*, 103:141–161, 2022.

[11] M. Koishi and S. Govindjee. Inverse Design Methodology of a Tire. *Tire Sci. Technol.*, 29(3):155–170, 07 2001.

[12] A. Albanesi, V. Fachinotti, Peralta. I., B. Storti, and C. Gebhardt. Application of the inverse finite element method to design wind turbine blades. *Compos. Struct.*, 161:160–172, 2017.

[13] A. Mira, A.K. Carton, S. Muller, and Y. Payan. A biomechanical breast model evaluated with respect to MRI data collected in three different positions. *Clin. Biomech.*, 60:191–199, 2018.

[14] A. Mazier, A. Bilger, A.E. Forte, I. Peterlik, J.S. Hale, and S.P.A Bordas. Inverse deformation analysis: an experimental and numerical assessment using the FEniCS Project. *Eng. Comput.*, 38:4099–4113, 2022.

[15] S. Govindjee and P.A. Mihalic. Computational methods for inverse finite elastostatics. *Comput. Methods Appl. Mech. Eng.*, 136(1):47–57, 1996.

[16] T. Yamada. Finite element procedure of initial shape determination for hyperelasticity. *Struct. Eng. Mech.*, 6(2):173–183, 1997.

[17] V.D. Fachinotti, A. Cardona, and P. Jetteur. Finite element modelling of inverse design problems in large deformations anisotropic hyperelasticity. *Int. J. Numer. Methods. Eng.*, 74(6):894–910, 2008.

[18] W. Hong. Inverse lagrangian formulation for the deformation of hyperelastic solids. *Extreme Mech. Lett.*, 9:30–39, 2016.

[19] X. Chen, C. Zheng, W. Xu, and K. Zhou. An Asymptotic Numerical Method for Inverse Elastic Shape Design. *ACM Trans. Graph.*, 33(4), jul 2014.

[20] J. Panetta, F. Isvoranu, T. Chen, E. Siéfert, B. Roman, and M. Pauly. Computational Inverse Design of Surface-Based Inflatables. *ACM Trans. Graph.*, 40(4), jul 2021.

[21] P. L. Chebyshev. Sur la coupe des vêtements. In *Assoc. franç. pour l'avancement des sci., Congrès de Paris*, pages 154–155, 1878.

[22] M. Servant. Sur l'habillage des surfaces. *C. R. Acad. Sci.*, 135:575–577, 1902.

[23] M. Servant. Sur l'habillage des surfaces. *C. R. Acad. Sci.*, 137:112–115, 1903.

[24] C. Mack and H. M. Taylor. The fitting of woven cloth to surfaces. *J. Text. Inst.*, 47:T477–T488, 1956.

[25] P. Howell, H. Ockendon, and J. Ockendon. Draping woven sheets. *The ANZIAM Journal*, 62:355–385, 2020.

[26] É. Ghys. Sur la coupe des vêtements: Variation autour d'un thème de tchebychev. *Enseign. Math.*, 57:165–208, 2011.

[27] R. S. Rivlin. The deformation of a membrane formed by inextensible cords. *Arch. Rational Mech. Anal.*, 2:447–476, 1958.

[28] A. C. Pipkin. Equilibrium of tchebychev nets. *Arch. Ration. Mech. An.*, 85:81–87, 1984.

[29] D. J. Steigmann and A. C. Pipkin. Equilibrium of elastic nets. *Philos. Trans. Royal Soc. A*, 335:419–454, 1991.

[30] A. C. Pipkin. Plane traction problems for inextensible networks. *Q. J. Mech. Appl. Math.*, 34:415–429, 1980.

[31] W. B. Wang and A. C. Pipkin. Inextensible networks with bending stiffness. *Q. J. Mech. Appl. Math.*, 39:343–359, 1986.

[32] G. Indelicato. The influence of the twist of individual fibers in 2d fibered networks. *Int. J. Solids Struct.*, 46:912–922, 2009.

[33] X. Peng, Z. Guo, T. Du, and W.R. Yu. A simple anisotropic hyperelastic constitutive model for textile fabrics with application to forming simulation. *Compos. B. Eng.*, 52:275–281, 2013.

[34] S. Mathieu, N. Hamila, F. Bouillon, and P. Boisse. Enhanced modeling of 3d composite preform deformations taking into account local fiber bending stiffness. *Compos. Sci. Technol.*, 117:322–333, 2015.

[35] M.A. Khan, T. Mabrouki, E. Vidal-Sallé, and P. Boisse. Numerical and experimental analyses of woven composite reinforcement forming using a hypoelastic behaviour. application to the double dome benchmark. *J. Mater. Process. Technol.*, 210(2):378–388, 2010.

[36] P. Harrison, R. Gomes, and N. Curado-Correia. Press forming a 0/90 cross-ply advanced thermoplastic composite using the double-dome benchmark geometry. . - *A: Appl. Sci. Manuf.*, 54:56–69, 2013.

[37] R. Nayak and R. Padhye. *Automation in Garment Manufacturing.* Woodhead Publishing, Duxford, 2017.

[38] N. Umetani, D. M. Kaufman, T. Igarashi, and E. Grinspun. Sensitive couture for interactive garment modeling and editing. In *ACM SIGGRAPH 2011 Papers*, SIGGRAPH '11, New York, NY, USA, 2011. Association for Computing Machinery.

[39] Y. Meng, P.Y. Mok, and X. Jin. Computer aided clothing pattern design with 3d editing and pattern alteration. *Comput. Aided. Des.*, 44(8):721–734, 2012.

[40] K. Wolff, P. Herholz, V. Ziegler, F. Link, N. Brügel, and O. Sorkine-Hornung. Designing personalized garments with body movement. *Computer Graphics Forum*, 42(1):180–194, 2023.

[41] P. Decaudin, D. Julius, J. Wither, L. Boissieux, A. Sheffer, and M. P. Cani. Virtual garments: a fully geometric approach for clothing design. *Comput. Graph. Forum.*, 25:625–634, 2006.

[42] K. Rose, A. Sheffer, J. Wither, M. P. Cani, and B. Thibert. Developable surfaces from arbitrary sketched boundaries. In *SGP '07*, page 163–172, 2007.

[43] A. Garg, A. O. Sageman-Furnas, B. Deng, Y. Yue, E. Grispun, M. Pauly, and M. Wardetzky. Wire mesh design. *ACM Trans. Graph.*, 33:1–12, 2014.

[44] A. O. Sageman-Furnas, A. Chern, M. Ben-Chen, and A. Vaxman. Chebyshev nets from commuting polyvector fields. *ACM Trans. Graph.*, 38:1–16, 2019.

[45] J. McCartney, B.K. Hinds, and K.W. Chong. Pattern flattening for orthotropic materials. *Computer-Aided Design*, 37(6):631–644, 2005. Comput. Aided. Des.

[46] A. Bartle, A. Sheffer, V.G. Kim, D.M. Kaufman, N. Vining, and F. Berthouzoz. Physics-driven pattern adjustment for direct 3d garment editing. *ACM Trans. Graph.*, 35(4), jul 2016.

[47] N. Pietroni, C. Dumery, R. Falque, M. Liu, T. Vidal-Calleja, and O. Sorkine-Hornung. Computational Pattern Making from 3D Garment Models. *ACM Trans. Graph.*, 41(4), jul 2022.

[48] J. Montes, B. Thomaszewski, S. Mudur, and T. Popa. Computational Design of Skintight Clothing. *ACM Trans. Graph.*, 39(4), aug 2020.

[49] J. Marsden and T. J. R. Hughes. *Mathematical foundations of elasticity*. Dover Publications, Inc., 1983.

[50] J. Cao, R. Akkerman, P. Boisse, J. Chen, H.S. Cheng, E.F. De Graaf, J.L. Gorczyca, P. Harrison, G. Hivet, J. Launay, et al. Characterization of mechanical behavior of woven fabrics: Experimental methods and benchmark results. *Compos. - A: Appl. Sci.*, 39(6):1037–1053, 2008.

[51] S. Mathieu, N. Hamila, F. Bouillon, and P. Boisse. Enhanced modeling of 3D composite preform deformations taking into account local fiber bending stiffness. *Compos. Sci. Technol.*, 117:322–333, 2015.

[52] M. Ferretti, A. Madeo, F. Dell'Isola, and P. Boisse. Modeling the onset of shear boundary layers in fibrous composite reinforcements by second-gradient theory. *Z Angew Math Phys*, 65:587–612, 2014.

[53] A.J.M. Spencer. Part iii. theory of invariants. *Continuum physics*, 1:239–353, 1971.

[54] A. Raoult. Symmetry groups in nonlinear elasticity: An exercise in vintage mathematics. *Commun. Pure. Appl. Math.*, 8(1):435–456, 2009.

[55] A.C. Pipkin. The relaxed energy density for isotropic elastic membranes. *IMA J. Appl. Math.*, 36(1):85–99, 1986.

[56] S.P. Boyd and L. Vandenberghe. *Convex optimization*. Cambridge University Press, 2004.

[57] A. Logg, Mardal, K.A., and G.N. Wells. *Automated Solution of Differential Equations by the Finite Element Method*. Springer, 2012.

[58] D. Balzani, P. Neff, Jörg Schröder, and G.A. Holzapfel. A polyconvex framework for soft biological tissues. adjustment to experimental data. *Int. J. Solids Struct.*, 43(20):6052–6070, 2006.

[59] C. Baek, A. O. Sageman-Furnas, M. K. Jawed, and P. M. Reis. Form finding in elastic gridshells. *Proc. Natl. Acad. Sci.*, 115:75–80, 2018.

[60] J. N. Hazzidakis. über einige eigenschaften der flächen mit constantem krümmungsmaass. *J. Reine Angew. Math.*, 88:68–73, 1880.

[61] A. Voss. über ein neues prinzip der abbildung krummer oberflächen. *Math. Ann.*, 19:1–26, 1882.

[62] S. L. Samelson and W. P. Dayawansa. On the existence of global tchebychev nets. *T. Am. Math. Soc.*, 347:651–660, 1995.

[63] Y. Masson and L. Monasse. Existence of global chebyshev nets on surfaces of absolute Gaussian curvature less than 2π. *J. Geom.*, 108:25–32, 2016.

[64] M Amabili. *Nonlinear mechanics of shells and plates in composite, soft and biological materials.* Cambridge University Press, New York, 2018.

[65] Y. Su, D. Riccobelli, Y. Chen, W. Chen, and P. Ciarletta. Tunable morphing of electroactive dielectric-elastomer balloons. *Proc. R. Soc. A: Math. Phys. Eng. Sci.*, 479(2276):20230358, 2023.

[66] P. Le Floch, X. Yao, Q. Liu, Z. Wang, G. Nian, Y. Sun, L. Jia, and Z. Suo. Wearable and washable conductors for active textiles. *ACS Appl. Mater. Interfaces*, 9(30):25542–25552, 2017.

[67] F. Momeni, S.M. Mehdi Hassani.N, and X. Liu. A review of 4d printing. *Mater. Des.*, 122:42–79, 2017.

[68] R.R Ruckdashel, D. Venkataraman, and J.H. Park. Smart textiles: A toolkit to fashion the future. *J. Appl. Phys.*, 129(13), 2021.

MOX Technical Reports, last issues

Dipartimento di Matematica
Politecnico di Milano, Via Bonardi 9 - 20133 Milano (Italy)

Burzacchi, A.; Rossi, L.; Agasisti, T.; Paganoni, A. M.; Vantini, S.
Commuting time as a determinant of higher education students' performance: the case of Politecnico di Milano

92/2023 Burzacchi, A.; Rossi, L.; Agasisti, T.; Paganoni, A. M.; Vantini, S.
Commuting time as a determinant of higher education students' performance: the case of Politecnico di Milano

90/2023 Gregorio, C.; Baj, G.; Barbati, G.; Ieva, F.
Dynamic treatment effect phenotyping through functional survival analysis

88/2023 Masci, C.; Spreafico, M.; Ieva, F.
Joint modelling of recurrent and terminal events with discretely-distributed non-parametric frailty: application on re-hospitalizations and death in heart failure patients

89/2023 Savaré, L.; Ieva, F.; Corrao, G.; Lora, A.
Capturing the variety of clinical pathways in patients with schizophrenic disorders through state sequences analysis

86/2023 Ferraccioli, F.; Sangalli, L.M.; Finos, L.
Nonparametric tests for semiparametric regression models

85/2023 Arnone, E.; De Falco, C.; Formaggia, L.; Meretti, G.; Sangalli, L.M.
Computationally efficient techniques for Spatial Regression with Differential Regularization

83/2023 Cavinato, L.; Massi, M.C.; Sollini, M.; Kirienko , M.; Ieva, F.
Dual adversarial deconfounding autoencoder for joint batch-effects removal from multi-center and multi-scanner radiomics data

82/2023 Pozzi, G.; Ciarletta, P.
Geometric control by active mechanics of epithelial gap closure

81/2023 Buchwald, S.; Ciaramella, G; Salomon, J.; Sugny, D.
A SPIRED code for the reconstruction of spin distribution